

Template Assisted *In situ* Synthesis of Ag@Au Bimetallic Nanostructures Employing Liquid Phase Transmission Electron Microscopy

Nabeel Ahmad,^{a*} Marta Bon,^{a*} Daniele Passerone,^b Rolf Erni^a

a) Electron Microscopy Center, Empa, Überlandstrasse 129, CH-8600, Dübendorf, Switzerland.

b) nanotech@surfaces, Empa, Überlandstrasse 129, CH-8600, Dübendorf, Switzerland.

*) These two authors contributed equally to this work and are co-first authors.

ABSTRACT: Noble metal nanostructure synthesis *via* seed-mediated route is a widely adopted strategy for a plethora of nanocrystal systems. Ag@Au core-shell nanostructures are radiolytically grown in real-time using *in situ* liquid-cell (scanning) transmission electron microscopy (LCTEM). Here we employ a capping agent, dimethyl-amine (DMA) and a coordinating complex, potassium iodide (KI) in an organic solvent (methanol) in order to: 1) slow down the reaction kinetics to observe mechanistic insights into the overgrowth process, 2) shift the growth regime from galvanic-replacement mode to direct synthesis mode resulting in the conventional synthesis of Ag@Au core-shell structures. A theoretical approach based on classical simulations complements our experiments providing further insight on the growth modes. In particular, we focus on the shape evolution and chemical ordering, as currently there is an insufficient understanding regarding mixed composition phases at interfaces of alloys even with well-known miscibilities. Furthermore, the comparison of theoretical and experimental data reveals that the final morphology of these nanoalloys is not simply a function of crystallinity of the underlying seed structure but instead is readily modified by extrinsic parameters such as additives, capping agent and modulation of surface energies of exposed crystal surfaces by the encapsulating solvent. The impact of these additional parameters is systematically investigated using an empirical approach in light of ab-initio simulations.

KEYWORDS: Ag@Au bimetallic core-shell nanostructures, template-mediated *in situ* synthesis, nucleation, kinetically controlled growth, liquid-cell TEM, molecular dynamics, DFT simulations.

There has been a phenomenal interest in the synthesis of noble metal nanostructures due to their interesting optical, catalytic and biomedical applications.^{1–4} Two of the most common such syntheses involves Au and Ag. In particular, Ag nanocrystals possess highly desirable plasmonic properties known as localized surface plasmon resonance (LSPR) making a strong case for their use in applications such as, *e.g.*, surface-enhanced Raman spectroscopy (SERS), biosensing.^{5–7} Ag nanoparticles especially with sharp corners can

give rise to strong electromagnetic fields resulting in an increase of Raman scattering cross-section of molecules at these specific sites.

The stability of Ag nanoparticles in terms of the oxidation of Ag⁺ ions is however a major issue for their practical applications. This can lead to the degradation of nanoparticle morphology negatively influencing their functional properties. Au on the other hand is a stable and inert material having an excellent resistance to oxidation, however

it is characterized by a plasmonic response of lower magnitude. Depositing few layers of Au on Ag does not alter the Ag identity of the nanoparticle bulk layers, thus preserving the plasmonic response, which is one order of magnitude stronger for Ag than Au. In this context, bimetallic Ag@Au core-shell nanostructures are intensely studied taking advantage of excellent plasmonic response of Ag and good chemical stability of Au.^{5,8,9} Such core-shell bimetallic nanoparticles also offer the opportunity to tune the LSPR peak from the visible to the near infrared spectrum range by manipulating the shape, size and composition of the structure.¹⁰ In addition to the tunability of the plasmonic properties, a composite nanostructure consisting of these two materials can give rise to attractive chemical and surface properties.¹¹ Ag@Au nanostructures are also of interest for use in biomolecular detection and biomedical diagnostics as they solve the problem of toxicity since the Au shell prevents direct contact of Ag during *in vivo* usage.¹²

The most frequent route utilized for the formulation of such hetero-structures is a seed-mediated protocol employing wet chemical synthesis.^{13,14} Regardless of its tremendous success, this procedure has mostly been restricted to those metals which do not undergo galvanic replacement reactions. This essentially implies that the reduction potential of the core metal should not be lower than the one of the deposited metal, unlike in the case of Ag@Au nanoparticles. This is especially true for conformal controlled deposition of Au over Ag, as the resultant galvanic reaction causes the formation of hollow nanoframes.¹⁵ Additionally Au deposited on Ag nanoparticles by means of galvanic replacement reactions suffers from two main core issues. Firstly, the coverage of Ag nanoparticles by Au is site specific, while secondly there is refilling of hollow nanoparticles by Au at increased concentrations causing the plasmonic properties to be dominated by Au instead of Ag.^{16,17} Despite of these difficulties several groups have been able to synthesize galvanic replacement-free Ag@Au nanostructures with morphologies such as nanorods, cubes and nanodisks.^{10,18,19}

A major challenge is to develop a mechanistic understanding of the growth of these complicated

nanostructures, because physical properties, *e.g.* the optical response, the catalytic activity and the magnetic behaviour, are highly dependent on the detailed composition and morphology.^{20,21} Usually a "quench and look" strategy is employed at intermediate stages of the reaction, however drying of the sample may result in a modified characteristics of the reactions coupled with missing of fast reaction dynamics.^{21,22} In the current context, *in situ* liquid cell transmission electron microscopy has emerged as a viable tool to understand nucleation and growth mechanisms of nanostructures.²³ The technique offers the opportunity to observe in real time self-assembly processes of nanocrystals, nucleation events and shape transformations of nanostructures in their native environment. Noteworthy, in the case of our liquid cell experiments, the electron beam is not only used as an imaging tool but can also stimulate dynamic processes in liquids through radiolysis. Basically, primary electrons create free radicals and aqueous electrons (e_{aq}^-) / solvated electrons (e_s^-) which can act as instigators to several different chemical reactions in the liquid at a rapid pace.^{24,25} This implies fast reaction dynamics making the overall observations very challenging.

In the case of Ag@Au core-shell nanostructures, the growth of the Au shell by means of galvanic replacement reactions or galvanic replacement-free reactions is greatly enhanced due to the modifications introduced by the radiolytic species induced under the electron beam. This results in the completion of the reactions within a matter of seconds rather than hours as observed on the bench in the absence of an electron beam.²⁶ Hence various oxidizing and reducing species introduced by the electron beam create additional reaction pathways transforming galvanic coupled reactions. The task of observing and interpreting such processes in real-time thus becomes very challenging. Recently, pH changes in the aqueous reaction solution have been implemented by Sutter *et al.* to modify and slow down reaction kinetics by quenching oxidizing species such as OH^\bullet in the solvent.^{26,27} Furthermore pH changes directly affect the concentrations of primary and secondary species. In the present study, we used a combination of capping strategy and modified solution chemistry to synthesize conventional Ag@Au nanostructures using two different seed templates

of Ag while additionally studying the effect of surface morphology on Au deposition. We chose to work with Ag nanocube and nanoplate morphologies rather than the more widely studied spherical one, because the non-spherical ones have recently shown to be promising for various applications.^{28–}

³⁰ Both templates are distinctive in their crystal symmetry (isotropic vs anisotropic), and growth modes.

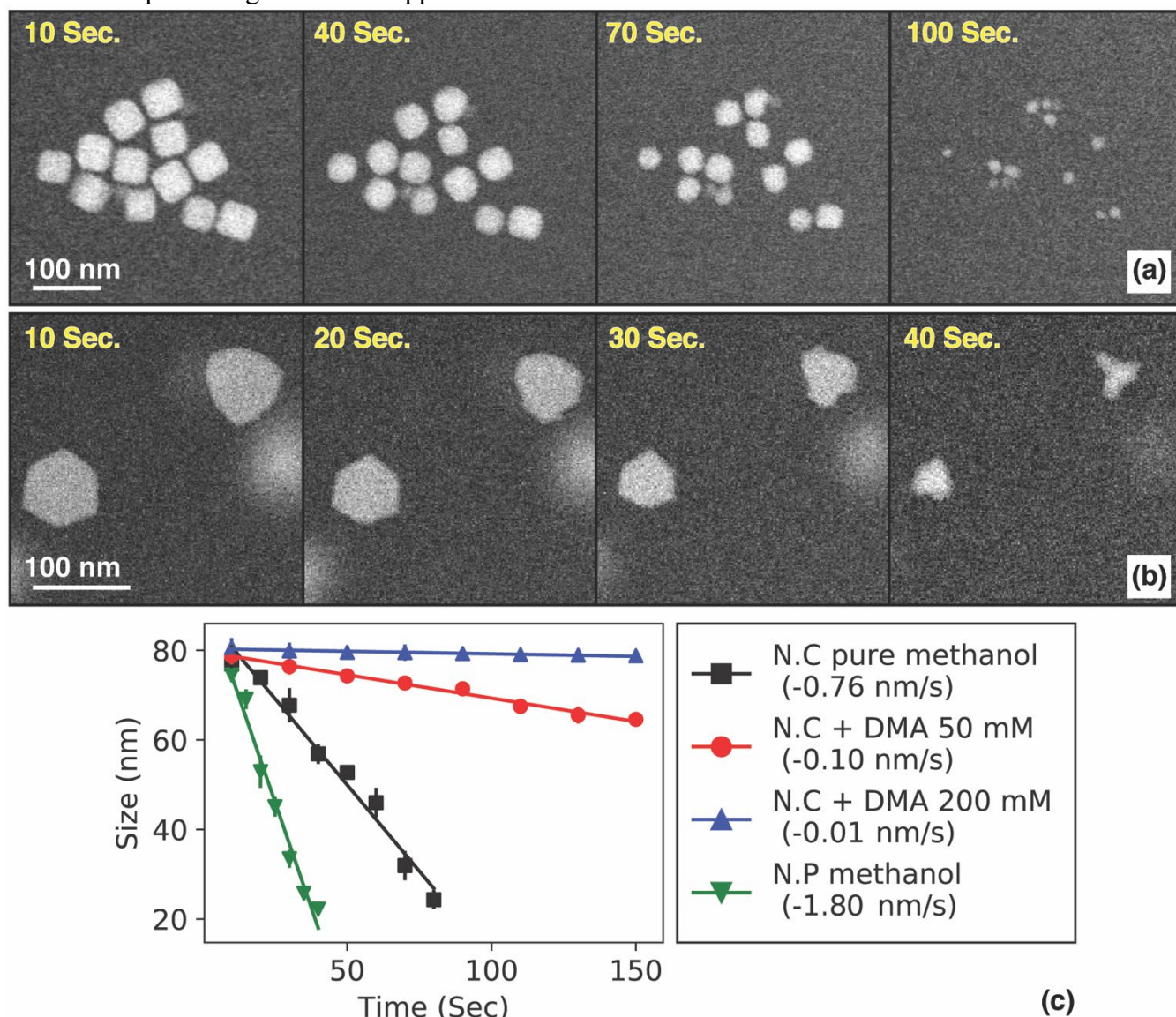


Fig 1: Dissolution of Ag template nanoparticles under the electron beam. (a) Time series of high-angle annular dark-field (HAADF) scanning transmission electron microscopy (STEM) images in methanol solvent showing etching by the electron beam of Ag nanocubes at $\dot{d} = 2.0$ electrons/ \AA^2 s. (b) Etching of triangular and hexagonal Ag nanoplates in methanol at similar doses as in (a). (c) Etching rate comparisons of Ag nanoparticle templates without DMA at $\dot{d} = 2.0$ electrons/ \AA^2 s and in DMA at $\dot{d} = 20.0$ electrons/ \AA^2 s showing a marked decrease in dissolution rate of Ag nanoparticles in later case (N.C: Nanocubes, N.P: Nanoplates).

The hexagonal/triangular 2D plates are often dominated by stacking faults or twins.³¹ and their 2D

growth is directly related to the stacking of planar defects (stacking faults/ twins) parallel to the

$\{111\}$ planes along which the growth is favored. On the other hand, the cubic nanocrystals of FCC (face centered cubic) metals are devoid of any planar defects and starting point is a truncated octahedron containing $\{100\}$, $\{110\}$ and $\{111\}$ planes on surfaces. The use of PVP for nanocube growth results in an altered growth rate for different facets transforming the octahedron morphology into cubic morphology. The resulting surfaces of the Ag nanocubes are therefore composed of large $\{100\}$ faces, $\{110\}$ edges and $\{111\}$ corners sites.³²

In addition to the experimental route, the characterization of nanoalloys growth can be tackled by atomistic simulations, *e.g.* classical molecular dynamics (MD). This technique allows for systematically controlling and disentangling the contributions coming from several players influencing the overall particle growth, *e.g.* lattice mismatch, surface energies, and rates of surface diffusion and adsorbate deposition. Following a commonly used computational protocol,³³ MD simulations were performed in gas phase at constant temperature, starting from a thermalized Ag seed. Au adatoms were deposited one by one at a constant rate from random positions, and between two subsequent depositions all atoms were free to move. As in the experiment, we considered two types of Ag seeds, *i.e.* Ag nanocubes and Ag nanoplates and we deposited a number of Au atoms equal to half of the initial seed size N , giving rise to final $\text{Ag}_N@\text{Au}_{N/2}$ NPs. The modelled NPs were constituted by thousands of atoms and the simulations sequences were of the order of microseconds, with deposition rates of about one atom/nanosecond. Modelling such kind of systems at an ab-initio level would have been unfeasible, and a classical description based on empirical potentials was required. More specifically, in this work we used the embedded atom model (EAM) parametrizations for Ag-Au alloys by Foiles and coworkers,³⁴ which we recently validated for the description of nanoalloys.⁶

We must point out at this stage that our computational model contains an important simplification.

While the experiment is conducted in liquid, the simulations are run in gas phase. However, this is mandatory due to the unavailability of an accurate force-field which properly captures simultaneously Ag-Au and the metal/liquid interactions. From one hand, even within the existence of such parametrization, the complexity of the experiment (*e.g.* the beam effect, the consequential presence of different radical species in solution, and the charge transfer phenomena) could not be represented by a classical model. On the other hand, a classical approach is needed in order to investigate processes occurring on long-time scales, such as the ones simulated. Nevertheless, even with this simplification, the performed MD simulations allowed for monitoring the shape evolution during growth and the chemical ordering inside the NPs and on the surface. These results are commented in light of our previous estimations for adsorption energies and diffusion barriers in Au-Ag heterodiffusion processes,⁶ and further insight is gained by performing ab-initio calculations. With this last treatment we investigated the interactions between Ag and the capping agent present in the experimental solution. For this purpose, we ran structural optimizations at the density functional theory (DFT) level and were able to explain the deviations of the classical simulations results from the experimental results, highlighting the important role of the additives in solution in determining the final nanoalloy shape.

The aim of this work is multifaceted. We first discussed the role of the beam in the experiment (*i.e.* NP etching and galvanic replacement). We then analyzed both experimentally and computationally the growth modes of the two templates (*i.e.* shape evolution and chemical ordering). Particular attention was paid to the influence of the presence/absence of different additives and of the pH conditions. All these considerations are of primary importance in order to design an efficient route for the direct synthesis of $\text{Ag}@\text{Au}$ NP.

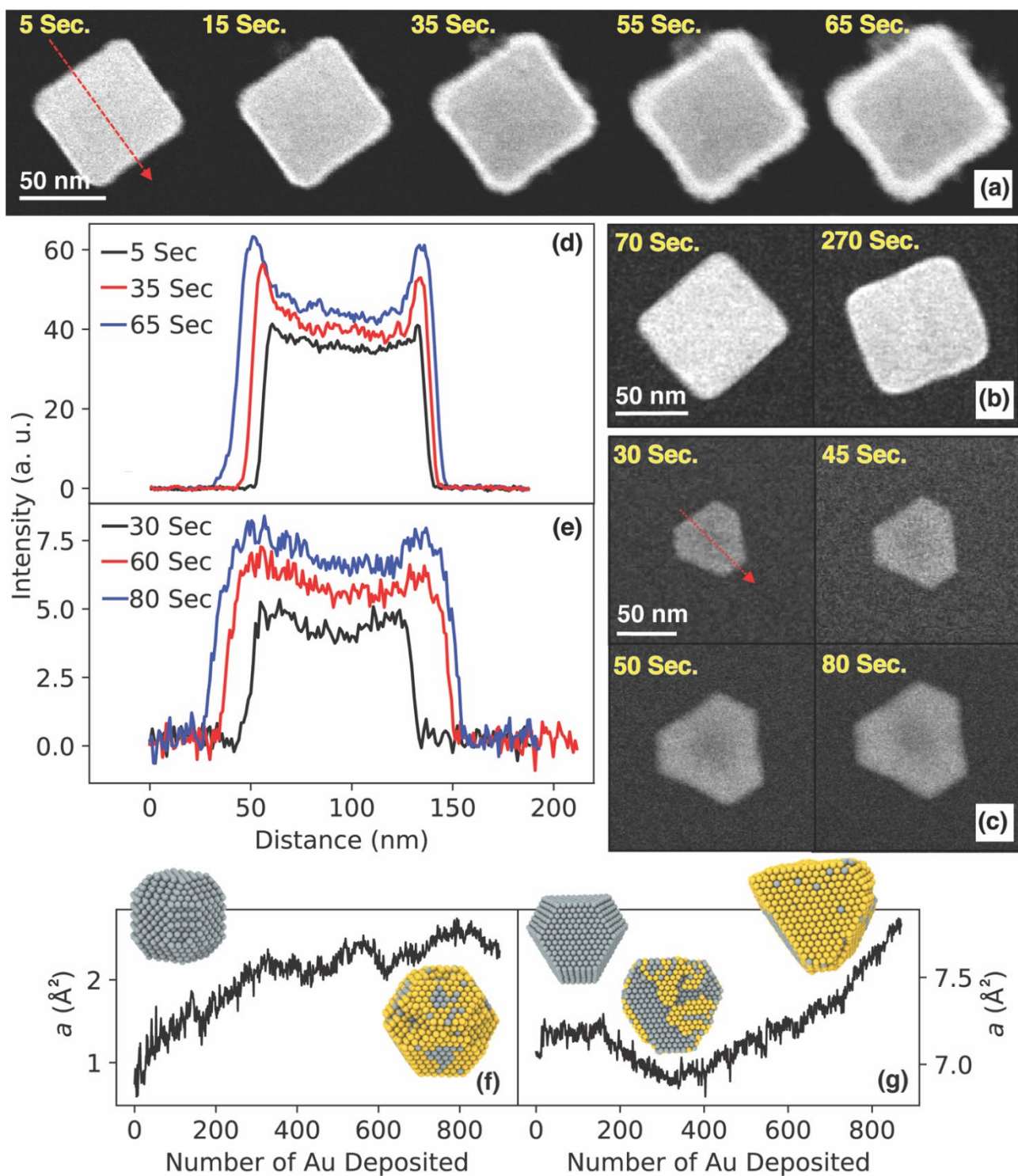


Fig 2: Shape Evolution of Cubic and Planar Morphologies. (a) Time resolved series of STEM-HAADF images showing growth of a conformal layer of Au over Ag nanocube at $\dot{d} = 20.0$ electrons/ $\text{\AA}^2\text{s}$ in methanol with 50mM DMA and KI. (b) Image of nanocube showing the thin epitaxial layer of Au over Ag in 200mM DMA and KI. (c) Formation of bimetallic Ag@Au nanoplates at $\dot{d} = 20.0$ electrons/ $\text{\AA}^2\text{s}$ (d) HAADF STEM intensity line profiles for Au deposition on the nanocube in (a). (e) HAADF STEM intensity line profiles at initial and final stages of Au deposition on the nanoplate in (c). (f-g) Data from MD simulations at 300K with deposition time equal to 2 ns. Asphericity parameter for cubic (f) and triangular (g) NPs.

RESULTS AND DISCUSSION

For the synthesis of Ag@Au nanostructures, we used methanol as an organic solvent. The primary products released during the radiolysis of methanol are solvated electrons (e^-_s) and methoxy radicals ($\text{CH}_3\text{O}^\bullet$).^{35,36} The former is a strongly reducing species while the latter is highly oxidizing similar to the case of e^-_{aq} and OH^\bullet in water radiolysis. For slowing down the reaction kinetics for *in situ* observations of the overgrowth mechanisms, the capping agent dimethylamine (DMA) was employed to stabilize the system. For direct synthesis of Ag@Au nanostructures in addition to DMA, potassium iodide (KI) was utilized as a coordinating ligand in small quantities.

Influence of Electron Beam on Ag Nanostructures. In their native media Ag nanoparticles were found to be very unstable under the electron beam as seen in Figure 1a, b. In a matter of seconds, the dissolution process starts causing the nanoparticles to etch away already after two minutes of constant beam irradiation at a relatively low electron dose rate (\dot{d}) of 2.0 electrons/ $\text{\AA}^2\text{s}$. This aggressive dissolution behaviour is triggered by the $\text{CH}_3\text{O}^\bullet$ radicals, which are the main oxidizing species of radiolysis in this system as otherwise, the Ag nanoparticles are quite stable in methanol for long periods with the beam blanked. Hence, it was critical to stabilize these Ag templates under the electron beam for sufficiently long periods to enable growth of Ag@Au core shell nanostructures. It was observed that when the Ag nanoparticles were

suspended in the primary amine (DMA), the etching was slowed down and it became possible to keep these nanoparticles stable for sufficiently long periods. This enabled us to make observations of dynamic processes using high magnifications at relatively high electron doses ($\dot{d} = 20.0$ electrons/ $\text{\AA}^2\text{s}$). Figure 1c compares the etch rates of the two morphologies with and without DMA effect. It can be seen in the plot that nanoplates etch at a rate 2.4 times faster than Ag nanocubes in the absence of DMA. This is likely due to the anisotropy and crystal defects in the structure of plates (stacking faults and twins) coupled with the higher surface to volume ratio of nanoplates at similar areal size ranges.³⁷ However, encapsulation of the nanoparticles in a methanol solvent containing 50 mM and 200 mM DMA, respectively, leads to drastically reduced etching rates as seen in Figure 1c, Figure S1 and Video S1.

Galvanic-Replacement Reactions in Ag@Au.

The introduction of very small concentrations of HAuCl_4 (100 μM) in the methanol solution containing the initial Ag seeds initiated galvanic-replacement reactions between Au and Ag at a rapid pace causing the complete hollowing out of the cubic nanoparticles in just under a minute at \dot{d} of 5.0 electrons/ $\text{\AA}^2\text{s}$. This is due to the high reduction potential difference between AuCl_4^- (0.99 V vs. standard hydrogen electrode (SHE)) and Ag (0.22 V vs. SHE), and to the large abundance of primary oxidizing species $\text{CH}_3\text{O}^\bullet$. As shown in Figure S2, the formation of the hollowed out nanocages with Au-rich frames at corners and edges proceeds by initiation of a hole at a large $\{100\}$ face of the nanocube and $\{111\}$ face of the nanoplates.

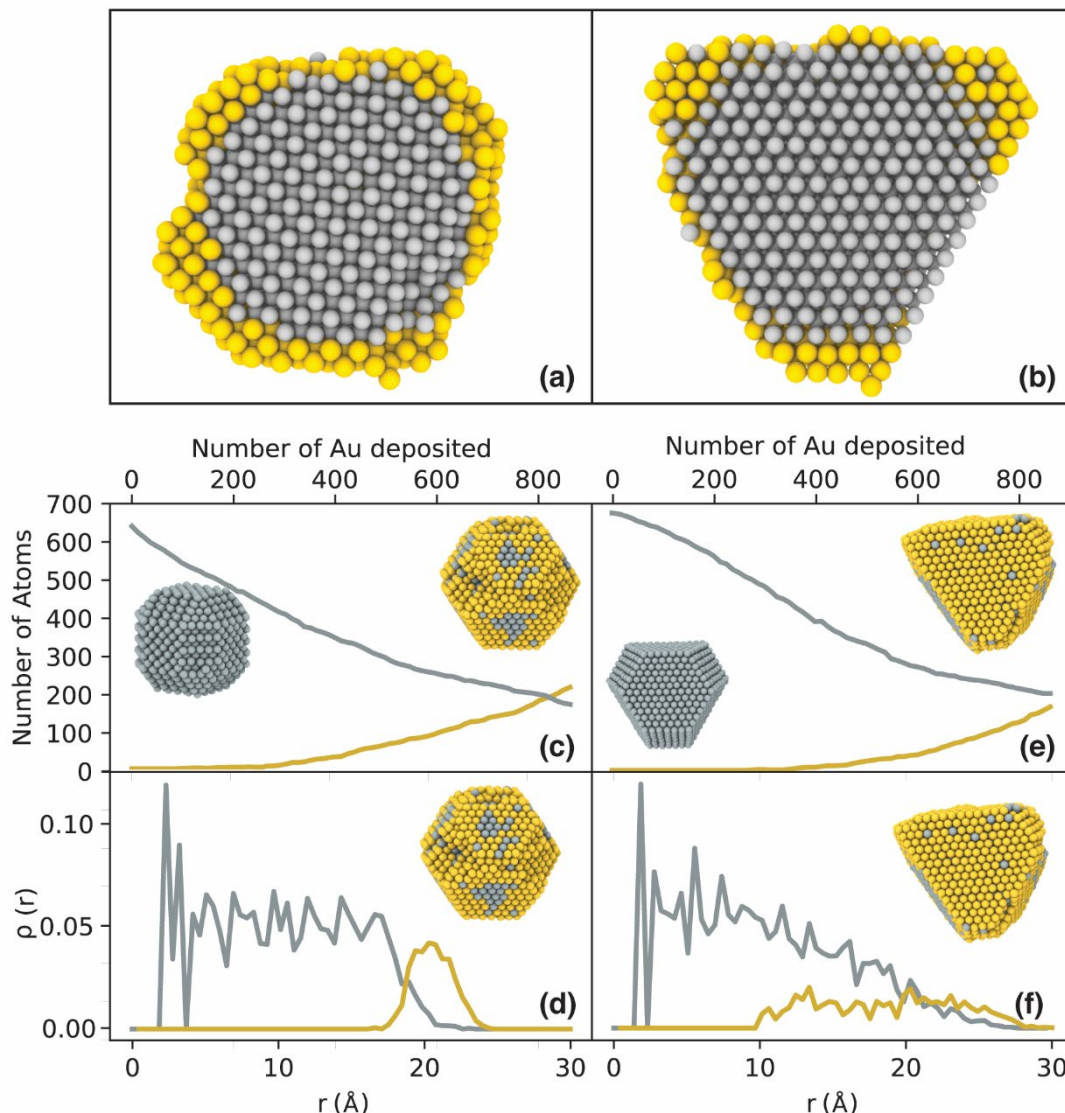


Fig 3: Surface analysis during the nanoalloy growth resulting from MD simulations. Left panels: cubic NP; right panels: triangular planar NP. (a-b) Cross-sectional view of the final nanoparticle configuration system. **(c-e)** Number of Ag atoms (silver curve) at the surface and number of Au atoms (gold curve) inside the NP. **(d-f)** Radial distribution functions of the last 5 equilibrated ns of $\text{Ag}_N\text{@Au}_{N/2}$ NP as function of the distance r from the NP center.

Literature³⁸ tends to attribute this behaviour to local defects at the large surfaces or defects in the coverage by PVP (polyvinyl pyridine) ligands used to stabilize the large exposed surfaces of the nanocrystal during formation of seeds. This is akin to an anode where Ag atoms are oxidized back into the solution by reduction of AuCl_4^- complexes which results in the formation of Au rich nanoframes. The present work mainly focuses on the strategy of preventing galvanic-replacement reactions and instead aims at directly synthesizing Ag@Au nanostructures.

Shape Evolution of Cubic and Planar Morphologies of Ag@Au. Figures 2a and 2c show the transformation of cubic and plate Ag templates into conventional (devoid of galvanic reaction) Ag@Au bimetallic nanostructures in methanol containing 50 mM DMA and 100 μM KI. It can be verified that there is no tell-tale hollowing of the nanoparticles from the central large faces as observed in the intensity line plot for hollow Ag@Au nanoparticle in Figure S3. This clearly points to the fact that galvanic-replacement reactions in the

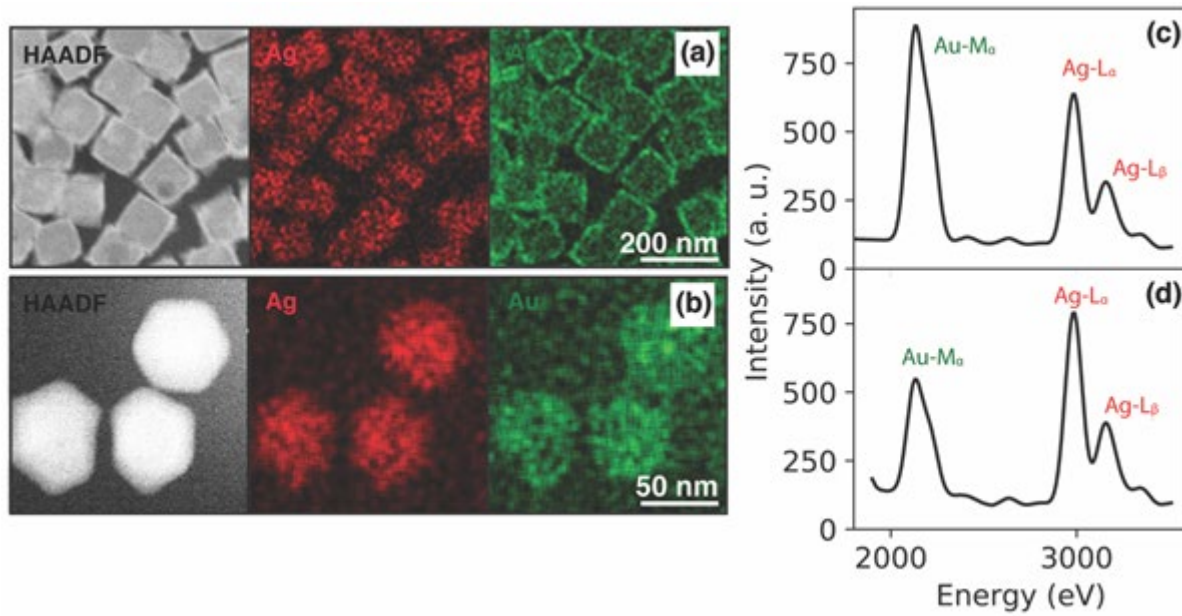


Fig 4: *In situ* EDS elemental distribution maps of conventional (absence galvanic replacement)Ag@Au nanostructures. (a) STEM-HAADF image of conventional Ag@Au nanocubes along with elemental distribution maps of Ag and Au. **(b)** HAADF STEM image of bimetallic Ag@Au nanoplates along with EDS maps showing the distribution Au and Ag. **(c)** EDS spectra showing characteristic peaks of Au and Ag from nanocubes. **(d)** Spectra from the associated bimetallic nanoplates in (b). Beam current (0.2 nA), frame size 512 x 512 pixels, dwell time of 400ns.

highly reactive environment of the liquid cell are largely inhibited by the presence of the additives. As it is clear from the comparison of the intensity line profiles in Figures 2d and 2e, the evolution of Ag nanocubes and nanoplates into Ag@Au nanostructures takes two distinct pathways. The line profiles of the nanocube (Figure 2d) significantly peaks at edges with time indicating growth along the entire $\{100\}$ surfaces. The experiment shows that cubic seed template seems to follow an epitaxial or layer-by-layer Au deposition at the initial stages, but undergo Volmer-Weber growth pattern at later growth stage (Figure S4).³⁹ This aspect is clearly deducible from the *in situ* movies (Video S2) of the growth since the initially smooth growth front becomes increasingly uneven at later stages.^{26,40} On the contrary, the plots associated with the nanoplate (Figure 2c) show a sizeable increase in thickness as well as lateral growth profile during the initial 60 s. After this early stage, the growth profile is mostly dominated by planar growth with a small thickness increase of the plate. Unlike nanocubes the nanoplate contain defects on side faces, therefore lateral growth is a dominant

factor. It however does not entail large $\{100\}$ faces for significant deposition in direction along the path of the beam, nevertheless a difference in contrast between the central part and the outer peripheral region can be observed showing the addition of Au as the plate grows.^{37,41}

Additional insight on the dynamics and on the chemical distribution (not directly accessible by experiment at the atomic level) within these nanostructures comes from atomistic simulations. MD trajectories allow for further tracking the NP shape evolution during the Au deposition, described using a macroscopic reaction coordinate, called asphericity (a). This is defined in terms of the three eigenvalues of the gyration tensor (S):

$$S = \begin{bmatrix} \sum_i (x_i^2 - x_{CM}^2) & \sum_i (x_i - x_{CM})(y_i - y_{CM}) & \sum_i (x_i - x_{CM})(z_i - z_{CM}) \\ \sum_i (x_i - x_{CM})(y_i - y_{CM}) & \sum_i (y_i^2 - y_{CM}^2) & \sum_i (y_i - y_{CM})(z_i - z_{CM}) \\ \sum_i (x_i - x_{CM})(z_i - z_{CM}) & \sum_i (y_i - y_{CM})(z_i - z_{CM}) & \sum_i (z_i^2 - z_{CM}^2) \end{bmatrix} \quad (1)$$

where x , y and z indicate the positions of the atoms (i) and of the center of mass (CM). A transformation to the principal axis system diagonalizes S :

$$S = \text{diag}(\lambda_1, \lambda_2, \lambda_3), \quad (2)$$

where we assume that the eigenvalues of S are sorted in descending order, *i.e.*, $\lambda_1 \geq \lambda_2 \geq \lambda_3$. The asphericity is defined as:

$$a = \lambda_1 - \frac{1}{2}(\lambda_2 + \lambda_3) \quad (3)$$

and indicates the deviation from a spherical symmetry^{42,43}: A value of $a=0$ corresponds to a sphere, while higher values to elongated structures. As expected and shown in Figures 2f, g, the asphericity a is smaller for the cubic seed compared to the triangular nanoplate, thus indicating the first one to exhibit the more isotropic morphology compared to the platelets. The trends of a as function of the number of atoms deposited show again that the

two NPs undergo different growth modes. More specifically, the cubic seed exhibits a more conformal growth, with a reaching almost instantaneously a plateau. On the contrary, during the initial stages of the triangular nanoplate growth, the NP becomes more spherulitic (*i.e.* the value of a decreases) and after this initial transient, the growth is planar (*i.e.* a increases abruptly and almost monotonically).⁴¹

Going back to the experiment, it is clear from Figure 2a that the final cubic NP presents a core-shell structure. The HAADF STEM image shows a distinct change in contrast arising from the deposition of Au around the nanocube (see also Video S2).

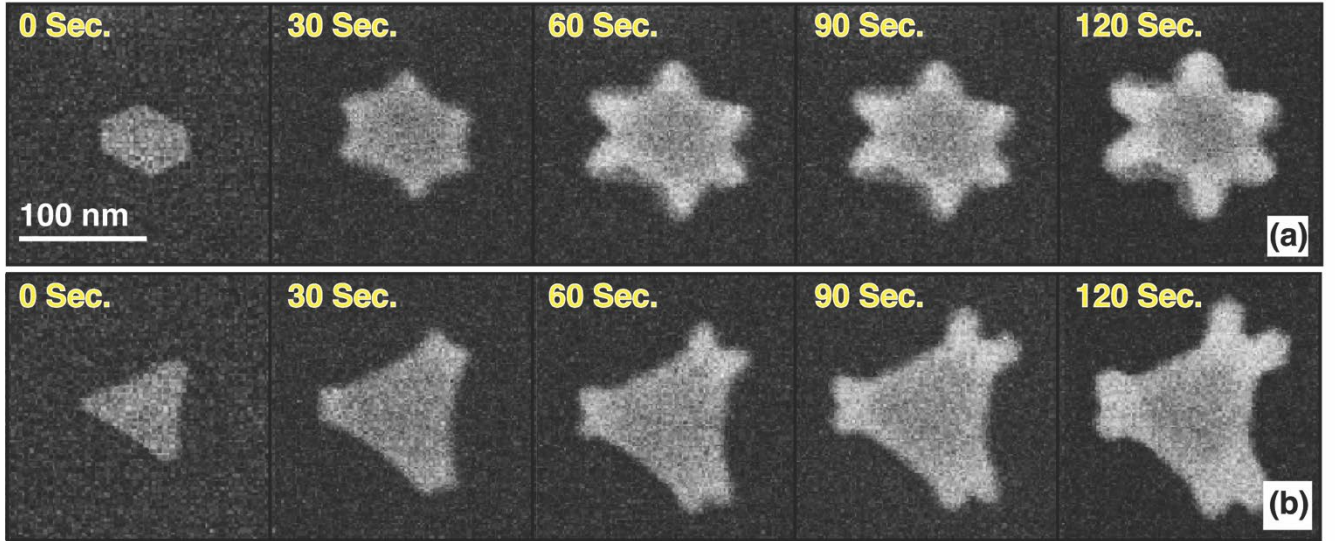


Fig 5: STEM-HAADF images showing shape evolution of Ag nanoplates under low capping agent and modified solution chemistry (10mM DMA, 100 μ M KI) at $\dot{d} = 2.8$ electrons/ \AA^2 s. (a) Time series of HAADF STEM images showing the shape evolution of Ag hexagonal nanoplate into bimetallic Ag@Au nanostars. (b) Formation of branches by Au deposition at the corner sites of Ag nanoprism.

This is due to the larger average atomic number (\bar{Z}) of the Au rich alloy forming on the surface of the nanocube. Instead, the deposition on the nanoplate is mostly restricted to the sides and corners (Figure 2c). A big difference in contrast is not recognized for the nanoplate, due to the moderate thickness of the template (21 ± 5 nm). The core-shell Ag@Au nanostructure is also recovered from MD simulations for both cube and plate. In addition to the qualitative analysis of the NP cross sections (Figures 3a and b), simulations allow a

quantification of the chemical ordering, by monitoring the radial distribution functions. These are function of the number of atoms of the two species ($n_{Au,Ag}$) in a shell at a distance between r and $r + \Delta r$, and indicate the distribution of distances of the atoms from the center of the seed:

$$\rho_{Au,Ag}(r) = \frac{n_{Au,Ag}(r)}{4\pi r^2 \Delta r}. \quad (4)$$

As shown in Figures 3d, f, Au atoms tend to remain in the outer shell in both NPs. In the case of the cube, the deposited Au atoms are sufficient to completely cover the NP surface and form a 1-2

atom thick layer around the Ag seed, while for the plate a complete coverage of the nanoplate was not reached at $\text{Ag}_N\text{Au}_{N/2}$ stoichiometry due to its higher surface-to-volume ratio with respect to the cube.

Chemical Ordering and Compositional Aspects of Ag@Au. The synthesized NPs were distinctively stable under the continuous irradiation by the electron beam. This made it possible to perform on Ag@Au bimetallic systems *in situ* quantitative energy dispersive X-ray spectroscopy (EDX) analysis. Usually the high electron doses required to generate sufficient counts causes uncontrollable growth of Au as well as numerous homogenous nucleation events in the viewing area, and for this reason EDX analyses are commonly done *ex situ*, where the drying process can result in unknown additional deposition and aggregation of the nanoparticles. After the growth of bimetallic nanostructures the supply of HAuCl_4 was stopped and only DMA with methanol was flowed into the cell for 30 min before conducting EDX analysis. Figure 4 shows EDX elemental distribution maps of directly synthesized or conventional (devoid of galvanic replacement) Ag@Au bimetallic nanostructures. In Figure 4a, it can be seen that Ag is mostly concentrated in the interior of the cubic templates while Au deposits are mostly concentrated on the faces and sides. EDX spectra show a larger concentration of Au vs Ag while the high contrast region are predominantly alloy of Au-Ag with a composition in the range of 60-70 at% Au (Figure S11). On the other hand, Ag nanoplates (Figure 4b) have reduced Au deposited under the same dose conditions. The associated EDX data also show a larger Ag concentration vs Au resulting in Ag rich composition. A line profile of the net intensities of Au and Ag from nanoplates also reflects this aspect (Figure S11). As the supply of Au was stopped to prevent uncontrolled growth of nanostructure, residual monomers still remained causing some increase in size as well as blunting and thickening of the nanoplates. This resulted in brighter contrast from the structure. These two aspects are clearly visible in the supplementary images (Figure S5). Additionally since the plates have a higher surface-to-volume ratio, acquiring discernible EDX signal required prolonged exposure to the electron beam. This had a negative ef-

fect as the 300 kV electron beam drives atom diffusion⁴⁴ subsequently resulting in merging of the nanoplates at later stage.

The differences in the amount of deposited Au under similar precursor concentrations and dose rates are most probably due to the characteristics of the facets exposed by the seeds. As known from literature and shown in Figures 3c and 3e, the largest surfaces exposed by the plates are {111}, which present the lowest adsorption energies for the Au adatom.⁶ In the (truncated) cube, these surfaces occupy the corners and the seed mainly exposes {100} and {110}, which are characterized by adsorption energies of about 30 and 40 meV larger compared to the {111}.⁶

Often, starting from core-shell configurations, fast diffusion phenomena lead to spontaneous alloying. Experimentally, we observed pronounced Ag diffusion towards the outer shell in cases where only DMA was used (Figure S6). The EDX intensity line plots in Figure S6 show overlapping of intensity peaks from Au and Ag which reveal that significant alloying had taken place. It was reported in recent studies^{5,16} that some amines like the hydroxylamine can reduce back the Ag atoms from the solution towards the nanoparticle surface but EDX mapping did not show any conclusive evidence for this matter. The Ag redistribution towards the shell region in case of nanocubes was observed throughout the cell in a short amount of time even in unexposed areas of the liquid cell, and therefore cannot be considered entirely due to beam driven phenomena (Figure S7, S8). Quantifying chemical ordering is very hard from the experiment. In order to shed further light on this aspect, we relied on the atomistic simulations. It was already mentioned that the general structure of the Ag@Au particles shows a thin Au external shell. Through that shell, Ag atoms can still diffuse to the surface. We characterized the Ag migration to the outer shell based on a common-neighbor analysis, as explained in ref⁴⁵. More specifically, atoms surrounded by more than 6 neighbors were considered to be inside the NP, while the others were targeted as belonging to the surface. Figures 3c and 3e show that the number of Au atoms inside the NP (the gold curves) progressively increases with the number of atoms deposited, simultaneously indicating a tendency for Ag to reach the

surface (silver line), behavior that we proved to be independent from the initial seed shape. The modelled data indicate thus the presence of the described migration events all along during growth; whether such diffusion would lead to a stable modification (alloying and / or surface segregation with the formation of islands) of the core-shell structure is a matter for further studies.

Influence of Additives on Growth Morphology.

The MD trajectories under thermodynamic conditions in absence of additives show a considerable increase of the {111} facets, because the diffusion from this surface is the fastest (associated to the lowest potential energy barrier) among all the inter-facets diffusion processes¹⁰. As a consequence, in the case of the cubic seed the {110} facets progressively disappear and the NP becomes a truncated octahedron, exposing mainly {100} and {111} facets, in agreement with previous studies.⁴⁶⁻⁴⁸ In contrast, the nanoplate adopts a more “triangular” morphology with a progressive regression of the {100} corners dimensions. This behavior is recovered at different Au deposition rates and system temperatures (Figures S16-S17). The final shapes resulting from simulation differ from the experimental nanostructures obtained in the presence of capping agents, whose effect cannot be easily taken into account in classical MD simulations of growth, mainly due to the absence of a proper force-field to describe the additional interactions.

For the just-mentioned reason, in the following we will separately (from the classical MD study) discuss the impact on deposition and final nanocrystal morphology of DMA and KI capping agents, in the light of experimental evidence and based on ab-initio calculations. As already seen in Figure S1, the suspension of Ag templates in DMA leads to their increased stability under the beam. This capping ligand works in two ways to promote the direct synthesis of Ag@Au. First, it physically forms a barrier that slows down the galvanic replacement reactions. Secondly, it sufficiently decreases the equilibrium concentration of Au monomer species in the solution,⁴⁹ similarly to other strong ligands, *e.g.* PVP.¹⁸ Indeed, we did not observe significant self-nucleation events in the presence of DMA as it would also serve the

same purpose of stabilizing metal precursor species. Several different factors can play a decisive role in terms of binding of capping agent to the seed surface, *e.g.* crystal structure, type of functional group and electronic properties. As already discussed, both nanocubes and nanoplates expose high-symmetry facets ({111}, {110} and {100}), characterized by different surface energies. The role of DMA was further elucidated by performing ab-initio DFT calculations of DMA adsorption on three low-index Ag surfaces, estimating the molecule adsorption energy:

$$E = E_{surf} + E_{ads} - E_{surf+ads}. \quad (5)$$

Here E_{surf} is the energy of the surface, E_{ads} is the energy of the DMA molecule in vacuum and $E_{surf+ads}$ indicates the energy of the system in which the molecule is adsorbed on the Ag substrate. E in Eq. (5) was further corrected for the basis set superposition error (BSSE) by using the counterpoise method proposed by Boys and Bernardi.⁵⁰ As shown in Figure S12, our calculations revealed that the only stable site for the molecule is “on-top” for all three slabs and that the adsorption occurs through N-Ag bond formation. The largest adsorption energy (corresponding to the most favourable adsorption site) is the one of the {100} which differs by 0.24 eV from the {110} Ag surface and by 0.09 eV from the {111}-termination (Table 1).

The adsorption process of DMA was compared with the one of a 2-pyrrolidone (2P) unit, which is a building block for the PVP polymer, an additive commonly used with the same goal of slowing down the kinetics of the reaction. For this purpose we modelled the adsorption of the 2P molecule following a similar protocol compared to the one of Al-Saidi and coworkers.⁵¹ In agreement with the experimental data and the previous calculations, 2P interacts with the surface *via* O-Ag and if possible *via* N-Ag bonds. For this reason, we defined the adsorbate position accordingly to the one of the O atom. As shown in Figure S12, on the {100} termination, the 2P binds “on-top” with N positioned close to the bridge site. On {110} the adsorption occurs in a long bridge position, and N occupies a position in between the short bridge and the top site. Finally, on the {111} termination, the most stable configuration is the (hexagonal closed packed) hcp-hollow site with N on a bridge.

As for the case of DMA, the most favourable termination is the {100}, showing an adsorption energy 0.28 eV and 0.10 eV higher than the one of the {110} and {111} faces. We notice that due to the double simultaneous interaction *via* O and N, the adsorption energies of 2P are always higher than the ones of DMA.

Table 1 Adsorption energies obtained at DFT PBE+D3/GTH/DVZP level and corrected using the counterpoise method.⁵⁰ Units in eV.

Ag termination	DMA	2P unit
{100}	0.92	0.99
{110}	0.68	0.71
{111}	0.83	0.89

Although the adsorption mechanism of DMA on Ag is different from the one of 2P, we can conclude that the trend in the binding affinity to the different Ag terminations shown by the two capping agents is very similar. This evidence is important in explaining the conformal Au deposition equally on all facets in the case of the nanocube. Note that, when using PVP in place of DMA, the degree of its polymerization is very important for obtaining nanoparticles with high aspect ratios. In the case of no polymerization (adsorption of the 2P monomer), irregular shapes with no preference for a specific orientation are observed [Sun, Y.*et al.*]⁵² As shown in Table 1, the 2P adsorption is energetically analogous to the DMA adsorption, corroborating the experimental results that no preference is observed for a particular high-symmetry face.

In the case of Ag nanoplates, the nanoparticles exhibit in addition a side face structure which incorporate stacking faults and twins resulting in anisotropic growth due to accelerated attachment of Au monomers at these high energy surfaces. Thus, the attachment sites for Au in the case of Ag nanoplates is not only restricted by the surface energies of the exposed facets but also by the high chemical potential of the side face structure. Potassium iodide KI works in a different way. According to Pearson's Hard-Soft Acid Base (HSAB) theory, it is essentially a coordinating ligand which interacts more strongly with AuCl_4^- complexes to form an additional complex namely AuI_4^- .^{18,53} In this case I^- binds more strongly to Au (III) than Cl^- . The resulting reduction potential of AuI_4^- is significantly lower (0.56 V vs SHE) as compared to AuCl_4^- .

By optimizing the relative concentrations of DMA and KI in the solution, tuning the morphology of these two types of Ag@Au nanostructures becomes possible. Figure S9 and Video S3 show a Ag nanocube under similar dose conditions \dot{d} of 20.0 electrons/ $\text{\AA}^2\text{s}$ but with a four times higher concentration of the capping agent (200 mM DMA). It can be seen that under this regime it takes significantly longer to form a thin epitaxial layer of Au on the surface of the Ag nanocube. Hence, the growth rate of Au layers can be easily tuned with this strategy and at the same time, it allows for slowing down the reaction kinetics tolerating an increased electron dose necessary to enhance the magnification.

Interestingly, reducing the amount of DMA to 10 mM in presence of 100 μM KI resulted in the formation of kinetically limited shape evolutions of the nanoplate seed crystal as seen in Figure 5. In Figure 5a at a relatively moderate \dot{d} of 2.8 electrons/ $\text{\AA}^2\text{s}$, we observed the growth of branches on the six corners of the hexagonal plates (Video S4). Hence, under this regime the deposition of Au atoms is much faster at these uncoordinated corner sites. This conclusion is also supported by previous deposition studies using different seed structures.^{40,54} Also in Figure 5b, the branches grow outwards from the truncated corners of the nanoprism. Under this regime the growth pathway of the seed crystal and thereby the shape taken by the product strongly depend on the respective ratios of monomer deposition rate *versus* the surface diffusion. When these rates are in balance, conformal growth can be expected resulting in uniform deposition on the edges and side faces. However, in cases where the rate of deposition is much higher than the surface diffusion, kinetically favoured growth such as that seen in Figure 5 is observed. At the end of the growth period, we could see rounding-off of the branches due to surface diffusion effects becoming dominant at later stages. This is due to the increasing chemical potential gradient between the convex and concave surfaces.⁵⁵

The role of KI in conjunction with DMA, even in minute quantity, was deemed to be necessary for the direct synthesis of Ag@Au nanostructures. In cases where only DMA was used with HAuCl_4

then introducing 0.5 mM HAuCl_4 precursor solution in the presence of 50 mM DMA resulted in significantly slower reaction kinetics and partially hollow Ag@Au nanoboxes and nanoplates were formed (Figure S7,S8). This clearly shows that, in spite of the presence of the capping agent on Ag, galvanic-replacement reactions are only partially inhibited. Both these additives complement each other during direct synthesis of Ag@Au .

As the impact of additives on the nanocrystal architecture was studied under the electron beam, it is very important to compare these results to real synthesis conditions. *Ex situ* experiments were performed outside the microscope with similar precursor and capping agent concentrations. The results are included as part of the supplementary information. Ag seeds were suspended into two solution chemistries, one containing DMA, KI while the other is devoid of the capping agent. The reactions under such regimes are considerably slow unlike under the electron beam where the free radicals are modifying the reaction rate. It was observed that partial galvanic replacement starts to take place only after 2 h of suspension in a Au precursor solution unlike in the liquid cell under electron irradiation where the reaction happens in under a minute. This clearly shows that methoxy radicals ($\text{CH}_3\text{O}^\bullet$) in methanol modify the galvanically coupled reactions. On the other hand, Ag particles suspended in Au solution containing DMA, KI largely remain intact even after 2 h in Au precursor solution (Figure S10). These results clearly indicate similar processes happening outside the microscope albeit at a much reduced pace due to the absence of electron beam effects. Therefore, the impact of additives in preventing galvanic replacement reactions could be confirmed and is demonstrated in the overlapped Au-Ag elemental distribution maps and associated line plots (Figure S11).

Effect of pH Changes on Synthesis Conditions. Previous work^{5,26} has shown that pH changes in the solution chemistry could potentially lead towards direct synthesis of bimetallic nanostructures of Ag@Au by increasing the reduction potential of the reducing agent. In that case, Au^{+3} is reduced by the reducing agent rather than by Ag atoms thereby blocking the galvanic replacement reactions. Interestingly OH^- ions from NaOH are also

known to modify not only the pH but the reduction potential of Au (III) precursors through ligand exchange causing suppression of galvanic reactions.⁵⁶ Yang *et al.* established the pH range for galvanic replacement free reduction for Ag@Au core-shell nanostructures.⁵ It was found that the addition of HAuCl_4 decreased the pH value of the solution. In their work, galvanic replacement-free deposition of Au over Ag was only observed at pH 9.69 and higher. However even at basic pH value of 9.54 voids were observed in Ag nanoparticles. Pure methanol is an organic solvent therefore direct pH measurements are an issue, however based on dissociation constant (pK_a) it has a slightly acidic character compared to water (pK_a 15.3 vs 15.5).⁵⁷ Therefore, the changes on pH values due to additives were carried out in reference to aqueous solutions. Additionally, the electron beam may slightly change the pH value.²⁵ We found the pH of 0.5 M of HAuCl_4 reference solution to be in the region of 4.5 making it slightly more acidic. Liquid cell studies in the past have shown that such variations could have a profound impact on the stability of Au nanoparticles in aqueous solutions.^{25,58} It was found that at low pH values Au nanoparticles etched away into the solution, while at pH 7 the particles were quite stable. At pH values above 10, coalescence of nanoparticles was observed. Interestingly amines like DMA are basic in nature. We found that the 50 mM DMA solution has a pH of 7.5 while KI in small quantities did not have a profound impact on that value. Further increase of the DMA concentration to 200 mM caused the pH to increase to 9.8. This is the range defined in the work of Yin *et al.* for galvanic replacement-free reactions using bench chemistry. In order to elucidate the role of DMA on galvanic reactions a control experiment was performed with NaOH to see if pH changes or capping effect of DMA was responsible for change in structure of the core-shell morphology. We still observed hollowing of Ag particles, although at a slightly reduced rate as compared to the acidic solution. Work conducted by Sun *et al.*,⁵⁶ observes galvanic replacement free deposition of Au in pH ranges 10.3-11.9 which is far higher than our case.⁵⁶ Based on this evidence we believe that the capping effect of DMA influences the growth of the Au shell in our experiments to a certain extent. However, as seen in Figures (S7 and S8), we still observed partial hollowing out of the nanocubes even

with high DMA concentration (pH 9.8). This shows that in our experiments KI was critical in the direct synthesis of Ag@Au nanostructures even at pH 7.5. The reason for partial galvanic replacement reactions even at high pH is most probably due to the modification introduced by the beam-induced radicals in the solution.

CONCLUSIONS

A systematic liquid-cell STEM study was carried out in order to understand growth evolution of Ag@Au nanostructures from two types of Ag seeds. The use of capping agent DMA in conjunction with KI made it possible to block galvanic replacement reactions completely. Under this growth regime, the equilibrium concentration of Au monomers and their reduction potential was significantly decreased. We observed that by changing the concentration of DMA, we could directly tune the growth rate of Au deposited on Ag. Higher concentrations of DMA resulted in lower deposition rates for Au under similar electron dose conditions. On the other hand, KI did not impact the deposition rate of Au. However, KI directly had an impact on the morphology of the resulting nanostructures. The use of DMA in itself did not completely stop galvanic reactions. It resulted in partially hollow structures with the bulk of Ag diffusing towards shell region while simultaneous addition of KI resulted in Au rich alloy on surface suppressing galvanic reactions for most part. A combination of such capping agents and coordinating complex in tandem turns out to be the best strategy to form stable Ag@Au nanostructures and to be able to study their dynamics under continuous high electron doses employed in LCTEM studies of inorganic nanomaterials.

Molecular dynamics simulations of nanoalloy growth starting from cubic and triangular Ag seeds, lead to $\text{Au}_{N/2}@\text{Ag}_N$ exhibiting NP onion-like structures, with Au mostly occupying the NP outer shells. Nonetheless, the calculations show a tendency of Ag to diffuse to the surface, which is independent from the initial seed shape. Finally, both theory and experiment show two different growth modes for the cubes and plates. The first undergo conformal 3d growth, while for the second, after an initial increase of the NP thickness, a

2d lateral growth is observed. Ab-initio calculations explain well the reason for conformal and non-site-specific deposition of Au as DMA adsorption is more or less uniform on all surfaces, with energy differences of the same order as in the PVP (the mostly used additive) monomer case. Existing literature shows that anisotropy sets in only upon PVP polymerization, thus reconciling with our DMA-assisted experiments.

In conclusion, critical insights derived from complex synthesis environment coupled with MD simulations would undoubtedly broaden the spectrum of synthesis strategies and understanding of Ag@Au nanostructures in particular.

METHODS

Ag Templates. Two types of Ag nanoparticle templates were used for the synthesis of Ag@Au nanostructures, namely Ag nanocubes and Ag nanoplates (thickness 21 ± 5 nm). The average size ranges for Ag nanocubes were 78 ± 5 nm while for Ag nanoplates was 70 ± 5 nm. The nanoparticles were centrifuged at 1300 rpm and subsequently decanted for 3 cycles in order to remove excess PVP from the solution, thus to avoid excess beam induced contamination of the sample.

Liquid Cell STEM Experiments. Liquid cell STEM experiments were carried out on a FEI Titan Themis 80-300 probe Cs-corrected microscope operated at 300 kV. A commercial liquid cell holder Poseidon 500 series by Protochips inc. was utilized for all liquid cell experimental work. A 2.5 μl droplet of the solution containing 1 mg/ml of Ag nanoparticle templates was deposited on a small e-chip containing 150 nm Au spacers. This suspension was sandwiched between two silicon-based e-chips with SiN electron-transparent windows. The two e-chips were placed in parallel providing a viewing area of approximately $550 \times 50 \mu\text{m}$. All *in situ* experiment were performed in STEM imaging mode using a high angle annular dark-field detector. Dose rates were manipulated by varying the gun lens, condenser aperture and magnification. STEM images were recorded at 1024×1024 pixels with dwell time of 4 μs while time series for videos were recorded at 512×512 pixels with dwell time of 6 μs .

EDX Analysis. The EDX maps are averaged maps using net intensities. The counts are on lower side overall as relatively low beam current (0.2 nA) was used to avoid damage by radiolysis. The scan series were acquired with a frame size of 512 x 512 pixels and a dwell time of 400ns over 396 frames. Low beam current generally resulted in lower counts requiring several minutes to acquire elemental maps. All mapping was done under similar dose conditions however the location of particles right next to side or corner of e-chip could also result in lower counts due to line of sight problems with detector (shadowing). We used double etched modified e-chips however the counts still varied from region to region within the cell.

Atomistic Simulations. Calculations were carried out with LAMMPS code.⁵⁹ The interactions between Au and Ag atoms were described by two the EAM parametrization of Foiles.⁴⁵ Simulations were performed in the NVT ensemble using the velocity rescaling thermostat,⁶⁰ at two different temperatures ($T_1 = 300$ K and $T_2 = 400$ K). The time step for the integration of Newton's equations of motion was set to 2 fs, while the deposition time interval varied in the 2-8 ns range. Post-processing calculations were performed using Plumed plugin.⁶¹ We modelled the "cubic" seed with a truncated cuboctahedron, made of {100} and {110} side facets with {111} corners. For the nanoplate we considered a seed mainly exposing {111} facets with {100} corners. It is worth noticing that the experimental seeds are of an average size range (about 70 nm) that cannot be easily treated fully-atomistically. Therefore, we scaled down the computational seeds size, and simulated NP of about 2000 atoms. A periodic box of 100 Angstrom side was used for the simulations.

Ab-initio Calculations. Calculations for the adsorption energies were conducted using PBE^{62,63} function using Grimme corrections for correctly capturing dispersion (PBE+D3). The valence electrons were treated explicitly using DZVP basis set,⁶⁴ whereas interactions with frozen atom cores were described with GTH pseudopotentials.⁶³ We set the charge density plane wave cutoff equal to 400 Ry, the convergence criterion to 10^{-7} a.u. for the wavefunction optimization and to 0.005 eV/Å for the forces. Adsorption energies were calculated on a 5x5x6 supercell {100} and {110} Ag

surfaces and on a 5x6x5 {111} Ag supercell. 10 Å vacuum were added on top of the surfaces and the bottom layer was kept fixed to bulk conditions. Calculations were run with ASE python library⁶⁵ interfaced using CP2K/6.0 calculator.⁶⁶ For each molecule (DMA and PVP), different inequivalent orientations on the surface plane and all the possible known adsorption sites were simulated, more specifically: Hollow, bridge, on-top for the {100}; Hollow, short-bridge, long-bridge, on-top for the {110}; Hollow-hcp, hollow-fcc; bridge, on-top for the {111}.

ASSOCIATED CONTENT

* Supporting Information

The Supporting information is free of charge available on ACS publication website.

In situ STEM movies (AVI), EDS analysis and additional experimental images, simulations at different temperatures and deposition rates, additional simulations using EAM parametrization by Zhou⁶⁷ (PDF)

The authors declare no competing financial interests.

AUTHOR INFORMATION

*E-mail: nabeel.ahmad@empa.ch

*E-mail: marta.bon@empa.ch

ACKNOWLEDGMENT

The authors acknowledge funding from ERC under EU's Horizon 2020 program (grant No. 681312).

REFERENCES

- (1) Skrabalak, S. E.; Chen, J.; Sun, Y.; Lu, X.; Au, L.; Cobley, C. M.; Xia, Y. Gold Nanocages: Synthesis, Properties, and Applications. *Acc. Chem. Res.* **2008**, *41*, 1587–1595.
- (2) Murphy, C. J.; Sau, T. K.; Gole, A. M.;

- Orendorff, C. J.; Gao, J.; Gou, L.; Hunyadi, S. E.; Li, T. Anisotropic Metal Nanoparticles: Synthesis, Assembly, and Optical Applications. *J. Phys. Chem. B* **2005**, *109*, 13857–13870.
- (3) Willets, K. A.; Van Duyne, R. P. Localized Surface Plasmon Resonance Spectroscopy and Sensing. *Annu. Rev. Phys. Chem.* **2007**, *58*, 267–297.
 - (4) Aiken, J. D.; Finke, R. G. A Review of Modern Transition-Metal Nanoclusters: Their Synthesis, Characterization, and Applications in Catalysis. *J. Mol. Catal. A Chem.* **1999**, *145*, 1–44.
 - (5) Yang, Y.; Liu, J.; Fu, Z. W.; Qin, D. Galvanic Replacement-Free Deposition of Au on Ag for Core-Shell Nanocubes with Enhanced Chemical Stability and SERS Activity. *J. Am. Chem. Soc.* **2014**, *136*, 8153–8156.
 - (6) Bon, M.; Ahmad, N.; Erni, R.; Passerone, D. Reliability of Two Embedded Atom Models for the Description of Ag@Au Nanoalloys. *J. Chem. Phys.* **2019**, *151*, 064105.
 - (7) Ghodselahi, T.; Arsalani, S.; Neishaboorynejad, T. Applied Surface Science Synthesis and Biosensor Application of Ag @ Au Bimetallic Nanoparticles Based on Localized Surface Plasmon Resonance. *Appl. Surf. Sci.* **2014**, *301*, 230–234.
 - (8) Sun, X.; Qin, D. Co-Titration of AgNO₃ and HAuCl₄: A New Route to the Synthesis of Ag@Ag–Au Core–Frame Nanocubes with Enhanced Plasmonic and Catalytic Properties. *J. Mater. Chem. C* **2015**, *3*, 11833–11841.
 - (9) Zhang, J.; Winget, S. A.; Wu, Y.; Su, D.; Sun, X.; Xie, Z.; Qin, D. Ag@Au Concave Cuboctahedra: A Unique Probe for Monitoring Au-Catalyzed Reduction and Oxidation Reactions by Surface-Enhanced Raman Spectroscopy. *ACS Nano* **2016**, *10*, 2607–2616.
 - (10) Krishnan, S. K.; Esparza, R.; Flores-Ruiz, F. J.; Padilla-Ortega, E.; Luna-Bárcenas, G.; Sanchez, I. C.; Pal, U. Seed-Mediated Growth of Ag@Au Nanodisks with Improved Chemical Stability and Surface-Enhanced Raman Scattering. *ACS Omega* **2018**, *3*, 12600–12608.
 - (11) Yoo, H.; Millstone, J. E.; Li, S.; Jang, J.; Wei, W.; Wu, J.; Schatz, G. C.; Mirkin, C. A. Core–Shell Triangular Bifrustums. *Nano Lett.* **2009**, *9*, 3038–3041.
 - (12) Mott, D.; Thuy, N. T. B.; Aoki, Y.; Maenosono, S. Aqueous Synthesis and Characterization of Ag and Ag–Au Nanoparticles: Addressing Challenges in Size, Monodispersity and Structure. *Philos. Trans. R. Soc. A Math. Phys. Eng. Sci.* **2010**, *368*, 4275–4292.
 - (13) Peng, Z.; Wu, J.; Yang, H. Synthesis and Oxygen Reduction Electrocatalytic Property of Platinum Hollow and Platinum-on-Silver Nanoparticles. *Chem. Mater.* **2010**, *22*, 1098–1106.
 - (14) Habas, S. E.; Lee, H.; Radmilovic, V.; Somorjai, G. A.; Yang, P. Shaping Binary Metal Nanocrystals through Epitaxial Seeded Growth. *Nat. Mater.* **2007**, *6*, 692–697.
 - (15) Lu, X.; Tuan, H. Y.; Chen, J.; Li, Z. Y.; Korgel, B. A.; Xia, Y. Mechanistic Studies on the Galvanic Replacement Reaction between Multiply Twinned Particles of Ag and HAuCl₄ in an Organic Medium. *J. Am. Chem. Soc.* **2007**, *129*, 1733–1742.
 - (16) Shahjamali, M. M.; Bosman, M.; Cao, S.; Huang, X.; Saadat, S.; Martinsson, E.; Aili, D.; Tay, Y. Y.; Liedberg, B.; Loo, S. C. J.; Zhang, H.; Boey, F.; Xue, C. Gold Coating of Silver Nanoprisms. *Adv. Funct. Mater.* **2012**, *22*, 849–854.
 - (17) Gao, C.; Lu, Z.; Liu, Y.; Zhang, Q.; Chi, M.; Cheng, Q.; Yin, Y. Highly Stable Silver Nanoplates for Surface Plasmon Resonance Biosensing. *Angew. Chemie Int. Ed.* **2012**, *51*, 5629–5633.

- (18) Gao, C.; Goebel, J.; Yin, Y. Seeded Growth Route to Noble Metal Nanostructures. *J. Mater. Chem. C* **2013**, *1*, 3898–3909.
- (19) Murshid, N.; Gourevich, I.; Coombs, N.; Kitaev, V. Gold Plating of Silver Nanoparticles for Superior Stability and Preserved Plasmonic and Sensing Properties. *Chem. Commun.* **2013**, *49*, 11355–11357.
- (20) Tsuji, M.; Matsuo, R.; Jiang, P.; Miyamae, N.; Ueyama, D.; Nishio, M.; Hikino, S.; Kumagae, H.; Kamarudin, K. S. N.; Tang, X.-L. Shape-Dependent Evolution of Au@Ag Core–Shell Nanocrystals by PVP-Assisted N,N -Dimethylformamide Reduction. *Cryst. Growth Des.* **2008**, *8*, 2528–2536.
- (21) Tan, S. F.; Lin, G.; Bosman, M.; Mirsaidov, U.; Nijhuis, C. A. Real-Time Dynamics of Galvanic Replacement Reactions of Silver Nanocubes and Au Studied by Liquid-Cell Transmission Electron Microscopy. *ACS Nano* **2016**, *10*, 7689–7695.
- (22) Sun, Y.; Xia, Y. Mechanistic Study on the Replacement Reaction between Silver Nanostructures and Chloroauric Acid in Aqueous Medium. *J. Am. Chem. Soc.* **2004**, *126*, 3892–3901.
- (23) Zhang, Y.; Keller, D.; Rossell, M. D.; Erni, R. Formation of Au Nanoparticles in Liquid Cell Transmission Electron Microscopy: From a Systematic Study to Engineered Nanostructures. *Chem. Mater.* **2017**, *29*, 10518–10525.
- (24) Woehl, T. J.; Evans, J. E.; Arslan, I.; Ristenpart, W. D.; Browning, N. D. Direct *In Situ* Determination of the Mechanisms Controlling Nanoparticle Nucleation and Growth. *ACS Nano* **2012**, *6*, 8599–8610.
- (25) Schneider, N. M.; Norton, M. M.; Mendel, B. J.; Grogan, J. M.; Ross, F. M.; Bau, H. H. Electron-Water Interactions and Implications for Liquid Cell Electron Microscopy. *J. Phys. Chem. C* **2014**, *118*, 22373–22382.
- (26) Sutter, E. A.; Sutter, P. W. *In Situ* Liquid Cell Electron Microscopy of Ag-Au Galvanic Replacement Reactions. *Nanoscale* **2017**, *9*, 1271–1278.
- (27) Sutter, E.; Jungjohann, K.; Bliznakov, S.; Courty, A.; Maisonhaute, E.; Tenney, S.; Sutter, P. *In Situ* Liquid-Cell Electron Microscopy of Silver-Palladium Galvanic Replacement Reactions on Silver Nanoparticles. *Nat. Commun.* **2014**, *5*, 1–9.
- (28) Ameer, F. S.; Varahagiri, S.; Benza, D. W.; Willett, D. R.; Wen, Y.; Wang, F.; Chumanov, G.; Anker, J. N. Tuning Localized Surface Plasmon Resonance Wavelengths of Silver Nanoparticles by Mechanical Deformation. *J. Phys. Chem. C* **2016**, *120*, 20886–20895.
- (29) Agrawal, A.; Kriegel, I.; Milliron, D. J. Shape-Dependent Field Enhancement and Plasmon Resonance of Oxide Nanocrystals. *J. Phys. Chem. C* **2015**, *119*, 6227–6238.
- (30) Li, W.; Zamani, R.; Rivera Gil, P.; Pelaz, B.; Ibáñez, M.; Cadavid, D.; Shavel, A.; Alvarez-Puebla, R. A.; Parak, W. J.; Arbiol, J.; Cabot, A. CuTe Nanocrystals: Shape and Size Control, Plasmonic Properties, and Use as SERS Probes and Photothermal Agents. *J. Am. Chem. Soc.* **2013**, *135*, 7098–7101.
- (31) Germain, V.; Li, J.; Ingert, D.; Wang, Z. L.; Pileni, M. P. Stacking Faults in Formation of Silver Nanodisks. *J. Phys. Chem. B* **2003**, *107*, 8717–8720.
- (32) Xia, Y.; Xiong, Y.; Lim, B.; Skrabalak, S. E. Shape-Controlled Synthesis of Metal Nanocrystals: Simple Chemistry Meets Complex Physics? *Angew. Chemie Int. Ed.* **2009**, *48*, 60–103.
- (33) Ferrando, R. Stress-Driven Structural Transitions in Bimetallic Nanoparticles. In *Frontiers of Nanoscience*; Elsevier Ltd., 2018; Vol. 12, pp 189–204.
- (34) Foiles, S. M.; Baskes, M. I.; Daw, M. S.

- Embedded-Atom-Method Functions for the Fcc Metals Cu, Ag, Au, Ni, Pd, Pt, and Their Alloys. *Phys. Rev. B* **1986**, *33*, 7983–7991.
- (35) Woehl, T. J.; Abellan, P. Defining the Radiation Chemistry during Liquid Cell Electron Microscopy to Enable Visualization of Nanomaterial Growth and Degradation Dynamics. *J. Microsc.* **2017**, *265*, 135–147.
- (36) Baxendale, J. H.; Wardman, P. The Radiolysis of Methanol: Product Yields, Rate Constants, and Spectroscopic Parameters of Intermediates. *NSRDS-NBS* **1975**, *54*, 1–26.
- (37) Lofton, C.; Sigmund, W. Mechanisms Controlling Crystal Habits of Gold and Silver Colloids. *Adv. Funct. Mater.* **2005**, *15*, 1197–1208.
- (38) Wang, Z. L. Transmission Electron Microscopy of Shape-Controlled Nanocrystals and Their Assemblies. *J. Phys. Chem. B* **2000**, *104*, 1153–1175.
- (39) Ahmad, N.; Wang, G.; Nelayah, J.; Ricolleau, C.; Alloyeau, D. Driving Reversible Redox Reactions at Solid-Liquid Interfaces with the Electron Beam of a Transmission Electron Microscope. *J. Microsc.* **2017**, *269*, 127–133.
- (40) Wu, J.; Gao, W.; Wen, J.; Miller, D. J.; Lu, P.; Zuo, J. M.; Yang, H. Growth of Au on Pt Icosahedral Nanoparticles Revealed by Low-Dose *In Situ* TEM. *Nano Lett.* **2015**, *15*, 2711–2715.
- (41) Alloyeau, D.; Dachraoui, W.; Javed, Y.; Belkahla, H.; Wang, G.; Lecoq, H.; Ammar, S.; Ersen, O.; Wisnet, A.; Gazeau, F.; Ricolleau, C. Unravelling Kinetic and Thermodynamic Effects on the Growth of Gold Nanoplates by Liquid Transmission Electron Microscopy. *Nano Lett.* **2015**, *15*, 2574–2581.
- (42) Vymětal, J.; Vondrášek, J. Gyration- and Inertia-Tensor-Based Collective Coordinates for Metadynamics. Application on the Conformational Behavior of Polyalanine Peptides and Trp-Cage Folding. *J. Phys. Chem. A* **2011**, *115*, 11455–11465.
- (43) Maroulis, G. Structure and Properties of Clusters: From a Few Atoms to Nanoparticles; *CRC Press*: Boca Raton, 2006.
- (44) Liu, Y.; Sun, Y. Electron Beam Induced Evolution in Au, Ag, and Interfaced Heterogeneous Au/Ag Nanoparticles. *Nanoscale* **2015**, *7*, 13687–13693.
- (45) Baletto, F.; Mottet, C.; Ferrando, R. Growth Simulations of Silver Shells on Copper and Palladium Nanoclusters. *Phys. Rev. B - Condens. Matter Mater. Phys.* **2002**, *66*, 1554201–15542011.
- (46) Sun, Y.; Xia, Y. Shape-Controlled Synthesis of Gold and Silver Nanoparticles. *Science*. **2002**, *298*, 2176–2179.
- (47) Xia, Y.; Xia, X.; Peng, H. C. Shape-Controlled Synthesis of Colloidal Metal Nanocrystals: Thermodynamic *versus* Kinetic Products. *J. Am. Chem. Soc.* **2015**, *137*, 7947–7966.
- (48) Baletto, F.; Mottet, C.; Ferrando, R. Molecular Dynamics Simulations of Surface Diffusion and Growth on Silver and Gold Clusters. *Surf. Sci.* **2000**, *446*, 31–45.
- (49) Yin, Y.; Alivisatos, A. P. Colloidal Nanocrystal Synthesis and the Organic–Inorganic Interface. *Nature* **2005**, *437*, 664–670.
- (50) Boys, S. F.; Bernardi, F. The Calculation of Small Molecular Interactions by the Differences of Separate Total Energies. Some Procedures with Reduced Errors. *Mol. Phys.* **1970**, *19*, 553–566.
- (51) Al-Saidi, W. A.; Feng, H.; Fichthorn, K. A. Adsorption of Polyvinylpyrrolidone on Ag Surfaces: Insight into a Structure-Directing Agent. *Nano Lett.* **2012**, *12*, 997–1001.

- (52) Sun, Y.; Xia, Y. Large-Scale Synthesis of Uniform Silver Nanowires Through a Soft, Self-Seeding, Polyol Process. *Adv. Mater.* **2002**, *14*, 833.
- (53) Datta, D. On Pearson's HSAB Principle. *Inorg. Chem.* **1992**, *31*, 2797–2800.
- (54) Zhang, H.; Jin, M.; Xia, Y. Noble-Metal Nanocrystals with Concave Surfaces: Synthesis and Applications. *Angew. Chemie Int. Ed.* **2012**, *51*, 7656–7673.
- (55) Ahmad, N.; Wang, G.; Nelayah, J.; Ricolleau, C.; Alloyeau, D. Exploring the Formation of Symmetric Gold Nanostars by Liquid-Cell Transmission Electron Microscopy. *Nano Lett.* **2017**, *17*, 4194–4201.
- (56) Sun, X.; Yang, Y.; Zhang, Z.; Qin, D. Mechanistic Roles of Hydroxide in Controlling the Deposition of Gold on Colloidal Silver Nanocrystals. *Chem. Mater.* **2017**, *29*, 4014–4021.
- (57) National Center for Biotechnology Information. PubChem Database. Methanol, CID=887 <https://pubchem.ncbi.nlm.nih.gov/compound/887> (accessed Apr 23, 2019).
- (58) Hermannsdörfer, J.; De Jonge, N.; Verch, A. Electron Beam Induced Chemistry of Gold Nanoparticles in Saline Solution. *Chem. Commun.* **2015**, *51*, 16393–16396.
- (59) Plimpton, S. Plimpton1995.Pdf. *Journal of Computational Physics*. 1995, pp 1–19.
- (60) Bussi, G.; Donadio, D.; Parrinello, M. Canonical Sampling through Velocity Rescaling. *J. Chem. Phys.* **2007**, *126*.
- (61) Tribello, G. A.; Bonomi, M.; Branduardi, D.; Camilloni, C.; Bussi, G. PLUMED 2: New Feathers for an Old Bird. *Comput. Phys. Commun.* **2014**, *185*, 604–613.
- (62) Perdew, J. P.; Burke, K.; Ernzerhof, M. Generalized Gradient Approximation Made Simple. *Phys. Rev. Lett.* **1996**, *77*, 3865–3868.
- (63) Krack, M. Pseudopotentials for H to Kr Optimized for Gradient-Corrected Exchange-Correlation Functionals. *Theor. Chem. Acc.* **2005**, *114*, 145–152.
- (64) VandeVondele, J.; Hutter, J. Gaussian Basis Sets for Accurate Calculations on Molecular Systems in Gas and Condensed Phases. *J. Chem. Phys.* **2007**, *127*.
- (65) Larsen, A. H.; Mortensen, J. J.; Blomqvist, J.; Jacobsen, K. W. The Atomic Simulation Environment—a Python Library for Working with Atoms. *J. Phys. Condens. Matter* **2017**, *29*, 273002.
- (66) Hutter, J.; Iannuzzi, M.; Schiffmann, F.; VandeVondele, J. Cp2k: Atomistic Simulations of Condensed Matter Systems. *Wiley Interdiscip. Rev. Comput. Mol. Sci.* **2014**, *4*, 15–25.
- (67) Zhou, X. W.; Johnson, R. A.; Wadley, H. N. G. Misfit-Energy-Increasing Dislocations in Vapor-Deposited CoFe/NiFe Multilayers. *Phys. Rev. B - Condens. Matter Mater. Phys.* **2004**, *69*, 1–10.

Insert Table of Contents artwork here

